ELSEVIER

Contents lists available at ScienceDirect

### Materials Science & Engineering A

journal homepage: www.elsevier.com/locate/msea





## Microscale deformation controlled by compositional fluctuations in equiatomic Nb–Mo–Ta–W alloys

Marta Pozuelo<sup>a,\*</sup>, Jaime Marian<sup>a,b</sup>

- a Dept. of Materials Science and Engineering, University of California Los Angeles, Los Angeles, CA, 90095, USA
- b Dept. of Mechanical and Aerospace Engineering, University of California Los Angeles, Los Angeles, CA, 90095, USA

#### ARTICLE INFO

# Keywords: High-entropy alloys In-situ SEM microcompression test Electron dispersive spectroscopy High-resolution TEM Edge dislocations

#### ABSTRACT

Local fluctuations in the chemical composition of high-entropy alloys (HEA) are known to have a significant influence on their mechanical performance. In this work, we conclusively establish a direct link between the strength of micron-sized specimens and deviations from equiatomic stoichiometry in body-centered-cubic (bcc) refractory Nb–Mo–Ta–W HEA. We perform a detailed electron dispersive spectroscopy (EDS) line profile analysis of the compressed micropillars after *in-situ* scanning electron microscopy microcompression tests at room-temperature and strain rates between  $10^{-4}$  and  $10^{-1}$  s<sup>-1</sup>. We find that compositional fluctuations near the micropillar tip is the best quantitative predictor of yield strength over strain rate and grain orientation. In micropillars tip rich in W, we measure a yield strength of 1500 MPa, while for those with a Ta and Nb-rich oscillations, the yield strength is 1000 and 700 MPa, respectively. Finally, our high-resolution TEM analysis reveals the presence of numerous edge dislocations, suggesting that deformation is controlled by nucleation due to the absence of sufficient internal sources.

#### 1. Introduction

The main idea behind the so-called 'high entropy' alloys (HEA) is to create materials with superior properties by combining a number of elements (typically five or more) in similar proportions and achieve solid solution phase stability through the large configurational entropy of the system. Due to the large chemical and configurational space available to create these materials, several hundred different HEA combinations now exist, each with their own distinct compositions, structure, and unique combination of properties [1–27].

Among the different systems proposed, refractory high entropy alloys (RHEA) are a special class of alloys composed of typically four or more refractory metal elements (Nb, Mo, Ta, V, W, Cr, Hf, Zr). While compositionally complex, these systems generally crystallize into a simple body-centered cubic (bcc) phase, found to be stable up to very high temperatures [9,17–25]. Similar to their pure bcc metal counterparts, RHEA may suffer from a lack of ductility in the low temperature regime [13,18]. However, they retain very high strengths at high temperatures, making them attractive candidates for high temperature structural applications, such as in the aerospace and nuclear industries [9,12]. Additionally, refractory metals such as Ta have been used in

many applications not only as electrical resistors and medical implants, but also as micro- and nano-electromechanical systems (MEMS and NEMS) [28]. Therefore, it might also be very interesting to apply RHEAs in the fabrication of micro- or nanodevices. Thus, it is important to understand how these RHEAs deform at the microscale and identify the governing mechanisms. In particular, RHEA display unusually high strength at high temperatures [18,24], above and beyond what might be expected of simple metals or alloys with an equivalent crystal lattice and microstructure.

Despite their apparent microstructural simplicity, however, experiments have shown that the strength and ductility of RHEAs can be significantly influenced by local chemical fluctuations (LCFs) [29–31]. One can envisage a multitude of plastic mechanisms that are highly dependent on the atomic environment, ranging from dislocation pinning [31], enhanced slip pathways and cross-slip [32–35], kink-pair nucleation [17,32–35], dislocation multiplication [29,30], etc. For that reason, any investigation of the peculiarities of plastic deformation in RHEA must necessarily capture the atomic scale. In this regard, size-scaling studies can be a useful tool to investigate unit mechanisms in small-scale pillars, 'starving' the material of volumetric dislocation sources and using the pillar diameter to set the length of the mobile

E-mail address: pozuelo@ucla.edu (M. Pozuelo).

<sup>\*</sup> Corresponding author.

dislocation sources. These experiments also provide a simple way to study single-crystal deformation to allow the investigation of the crystallographic orientation dependence. However, while these studies provide an ideal validation testbed for the models due to the simplicity in geometry and loading conditions, only a handful of such studies exist for Nb-Mo-Ta-W alloys [19,26,27]. Despite much work remaining to be done to transfer the understanding gained in small scale bcc RHEA tests to macroscale applications, the extraordinary properties measured in micropillars, such as strength and ductility [19,26] and the remarkable thermal stability of nanocrystalline micropillars [27], are a very encouraging sign of the potential of these alloys as engineering materials. Similarly, no measurements of strain rate sensitivity -usually a reliable indicator of dynamic strain ageing (DSA)- exist for single crystals of these alloys at room temperature. Although DSA has been reported at room and lower temperatures, leading to the characteristic serrated plastic flow behavior in the stress-strain curve of small-scaled NbMoTaW RHEA pillars [26,36].

In this work, we carry out *in-situ* scanning electron microscopy (SEM) microcompression tests to investigate the mechanical behavior of Nb–Mo–Ta–W RHEA, and to establish a connection between the wavelength of LCFs and specimen strength. All tests have been conducted at room-temperature and strain rates between  $10^{-4}$  and  $10^{-1}$  s $^{-1}$ . The compressed pillars are further analyzed using electron dispersive spectroscopy (EDS) line profile analysis to extract chemical composition profiles. Finally, we examine the deformed microstructure by high-resolution TEM (HRTEM). In the following we provide a description of the experimental methods, followed by the results, a discussion, and the conclusions.

#### 2. Experimental procedure

Elementary powders of Nb (16.8 wt%), Mo (17.3 wt%), Ta (32.7 wt%) and W (33.2 wt%) were arc melted together to attain the nominal atomic composition of Nb $_{25}$ Mo $_{25}$ Ta $_{25}$ Wo $_{25}$ . After arc casting, in the assolidified condition, these alloys are known to display a dendritic heterogeneous microstructure. Therefore, a heat treatment in vacuum was performed at temperatures around 1700 °C for 1 week to obtain a homogenized single-phase alloy. Arc casting and the secondary heat treatment were performed at Materials Preparation Center at Ames Laboratory.

Samples were cut from the provided buttons and subsequently grounded by #120, #400 and #1200-grit SiC sandpaper sheets in sequence, before wet-polishing with 1, 0.3 and 0.05  $\mu m$  Al $_2O_3$  suspensions. Polished samples were etched with Nital to reveal their microstructure. The morphology and composition of the RHEAs were investigated with scanning electron microscopy (SEM) using a FEI Nova 230 Variable Pressure SEM (VP-SEM) equipped with a Thermo Fisher Scientific Electron Dispersive Spectroscopy (EDS) system. An accelerating voltage of 15 kV, a working distance (WD) of around 5 mm and the dwell time per pixel between 2 and 2.2 s (depending upon the number of counts) were the optimal settings to minimize the scatter in the EDS data

The theoretical limit of EDS detection is about 0.1 wt% under the optimal experimental settings (flat polished surface of the specimen, adequate beam current and X-ray signal) [37]. As predicted by Kanaya-Okayama calculations [38] the radius of the interaction volume not only depends on the electron beam energy but also decreases with the atomic number of elements and the density of the specimen as well as the tilt angle of the specimen surface. Therefore, in our case having very heavy elements such as W and Ta and considering that the specimen surface was tilted  $52^{\circ}$ , we expect an interaction volume smaller than 1  $\mu$ m. In fact, we measured a EDS spot size around 0.5  $\mu$ m after the irradiation damage on our sample (See Supplementary Fig. S1).

Single crystal micropillars with 1  $\mu m$  in diameter and 1:3 and 1:4 aspect ratios were machined using a focused ion beam (FIB) operated at 30 kV from different grains of the RHEA samples. The machining was

carried out applying a series of concentric annular milling patterns with different currents. In order to obtain the desired micropillar shape and minimize tapering, a low beam current (0.3 nA) was used as final milling step. FEI Nova 600 Nanolab Dual-Beam Focused Ion Beam - Scanning Electron Microscope (FIB-SEM) was used for the sample preparation. We measured tapering angles  $<\!5^{\circ}$ , which are in good agreement with the values reported in the literature for micropillars machined by FIB [39–47]. However, in order to avoid any overestimation of the measured stress due to the tapering, the diameter was considered at half-height of the pillar ( $\sim\!1~\mu m$ ).

The mechanical behavior of RHEAs micropillars was studied using in-situ SEM microcompression test by means of a PI 85 SEM PicoIndenter (Hysitron Inc.) with a 5  $\mu$ m flat punch diamond probe. These experiments were conducted at room temperature (RT) under displacement control mode and at strain rates between  $10^{-4}$  to  $10^{-1}$  s $^{-1}$ .

Finally, we performed a detailed post-mortem characterization using high-resolution transmission electron microscopy (HRTEM) of at least one of the characteristic compressed micropillars within each grain to determine their orientation and to investigate the deformation mechanisms during compression. A FEI Titan 300-kV scanning transmission electron microscope (STEM) was used for this purpose.

#### 3. Results

#### 3.1. Microstructural characterization of the bulk RHEA sample

Fig. 1a shows the microstructural characterization of the bulk RHEA sample before etching to obtain a reference EDS analysis. A line profile examination was performed along the red arrow of 450-µm length that traverses several grains. Fig. 1b displays the EDS measurements in at. % of Nb-L, Mo-L, Ta-L, and W-M as a function of position along the length of the red arrow highlighted in Fig. 1a. Even though Mo at. % (gray curve) is stoichiometrically uniform, it is interesting to note the compositional oscillations between neighboring grains. While Ta at. % (red curve) is mainly the highest in concentration, there are grains rich in W (blue curve) that are also poor in Nb (green curve). An equiaxed microstructure with an average grain size around 140  $\pm$  15  $\mu m$  was revealed after etching as can be seen in Fig. 1c. The at. % concentration obtained from the spot analysis from a total of 14 arbitrary grains (three of those grains are enclosed and highlighted in Fig. 1c) is shown in Fig. 1d. On average, the composition variations measured from the 14 grains (Fig. 1d) are 22.1  $\pm$  1.9, 26.3  $\pm$  1.9, 24.1  $\pm$  1.6 and 27.5  $\pm$  3.0 at. % for Nb, Mo, Ta and W, respectively where the errors are the standard deviation of the average. Fig. 1e shows the SEM image of an individual grain (grain #3) where some of the FIB machined micropillars are also visible. The line profile was taken along the red arrow of around 10  $\mu m$ length from the bulk. As can be seen in Fig. 1f, the compositions are fluctuating along the stoichiometric concentrations (25 at. % concentration is highlighted by a dashed black line). It can be noticed that Ta composition is the greatest component along the first 2 µm of the line profile and then decreases below the stoichiometric concentration to be again at the top of this profile for approximately the next 2 µm. W concentration is the highest on those Ta valleys. While Nb follows closely the stoichiometric concentration, Mo is below that for practically the entire line profile. These fluctuations within an individual grain indicate that the micropillars composition depends on their location within the grain. These images essentially reveal the various length scales inherent to the alloy composition, which will play a crucial role in the results presented next.

#### 3.2. Mechanical characterization of RHEA micropillars

To study the mechanical behavior of the alloy, in-situ SEM

<sup>&</sup>lt;sup>1</sup> The letters L and M refer to the energy emission lines.

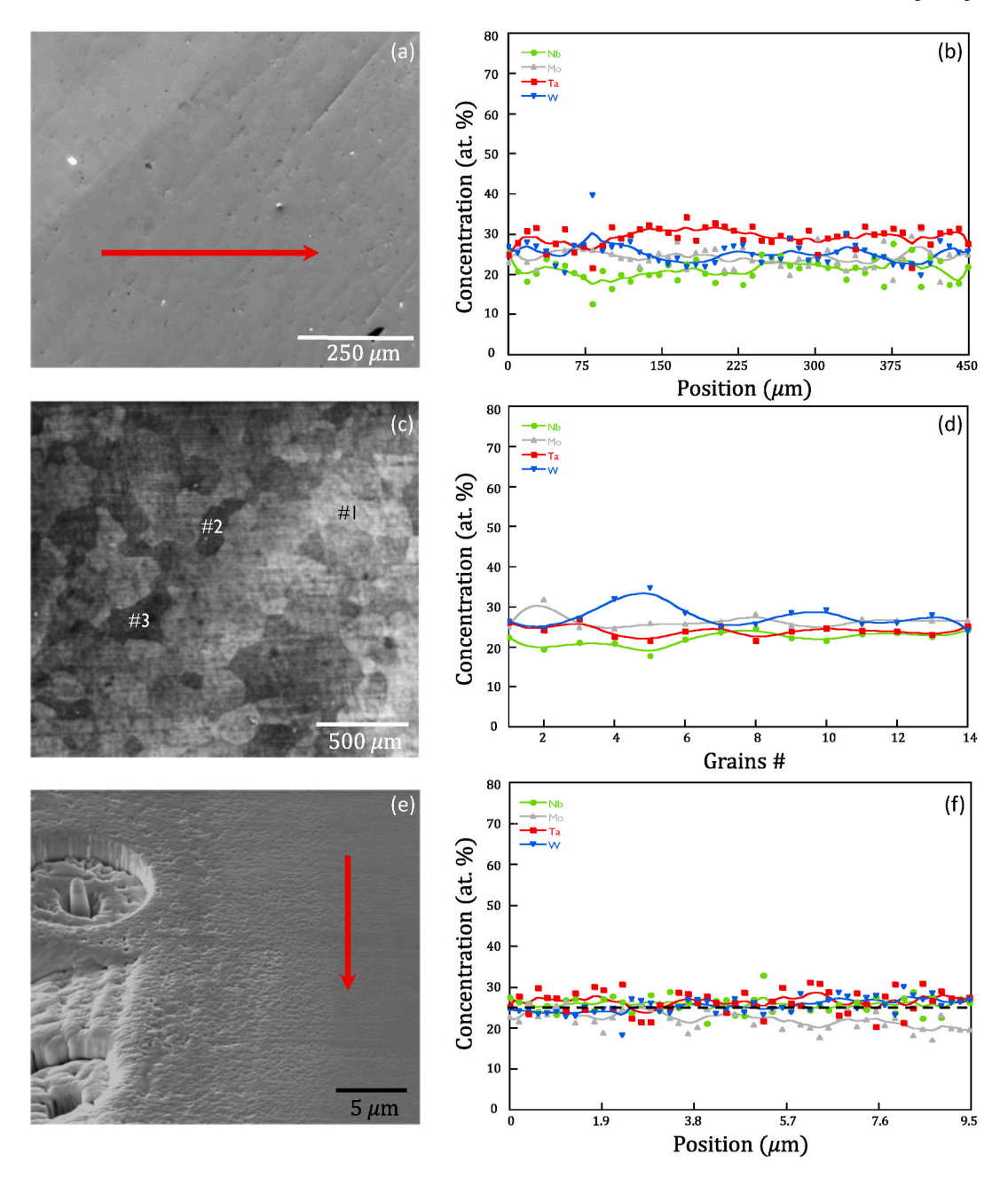


Fig. 1. (a) SEM image of the RHEA sample before etching. (b) Line profile EDS analysis showing the Nb, Mo, TA and W concentrations in at. % vs. the position along the red arrow in (a). (c) SEM image of the RHEA after etching showing its microstructure. (d) EDS spot analysis taken from 14 different grains. (e) 52° tilted-view SEM image at higher magnification displaying a few machined micropillars within a grain. (f) Line profile EDS analysis along the red arrow shown in (e). (For interpretation of the references to color in this figure legend, the reader is referred to the Web version of this article.)

microcompression tests were performed on single crystal 1- $\mu$ m micropillars at RT and at strain rates between  $10^{-4}$  to  $10^{-1}$  s<sup>-1</sup>. The characteristic stress-strain curves at different strain rates can be seen in Fig. 2. Legend labels as "GxPy" mean Pillar #y from Grain #x.

As expected from the compositional variations in the RHEA microstructure noted in Fig. 1, the microcompression test results show a remarkable scatter in the data. Fig. 2a shows the stress-strain curves at  $10^{-4}\,{\rm s}^{-1}$  of micropillars from two different grains. The curves belonging to grain #3 display yield strength values between 900 and 1400 MPa, while the curves from grain #5 show an average yield strength of 1200  $\pm$  30 MPa.

As well, the elastic modulus seems to decrease with decreasing yield strength for pillars from the same grain, as for example in the curves from grain #3 (G3P5, G3P1, G3P7 and G3P6) at a strain rate of  $10^{-4} \, {\rm s}^{-1}$ .

In fact, our results show almost two-times lower slope for the softest pillar (G3P6) than that for the strongest one (G3P5). These results suggest a direct association between elastic modulus and yield stress, with softer pillars always being less stiff and vice versa.

The stress-strain curves at  $10^{-3}\,\mathrm{s}^{-1}$  of micropillars from two different grains are shown in Fig. 2b. The curves for grain #2 display yield strength values between 980 MPa (G2P5) and 1600 MPa (G2P2), while values between 1150 MPa (G5P5) and 1600 MPa (G5P4) are measured for grain #5. Fig. 2c displays the curves at  $10^{-2}\,\mathrm{s}^{-1}$  of strain rate for pillars from three different grains, with yield strength values between 590 (G0P7) and 975 MPa (G0P9) for grain #0, 975 (G1P2) and 1600 (G1P3) MPa for grain #1, and around 1000 MPa (G5P1 and G5P3) for grain #5. Finally, Fig. 2d displays the results at  $10^{-1}\,\mathrm{s}^{-1}$  for pillars all from grain #2. Two groups can be clearly distinguished: one, the

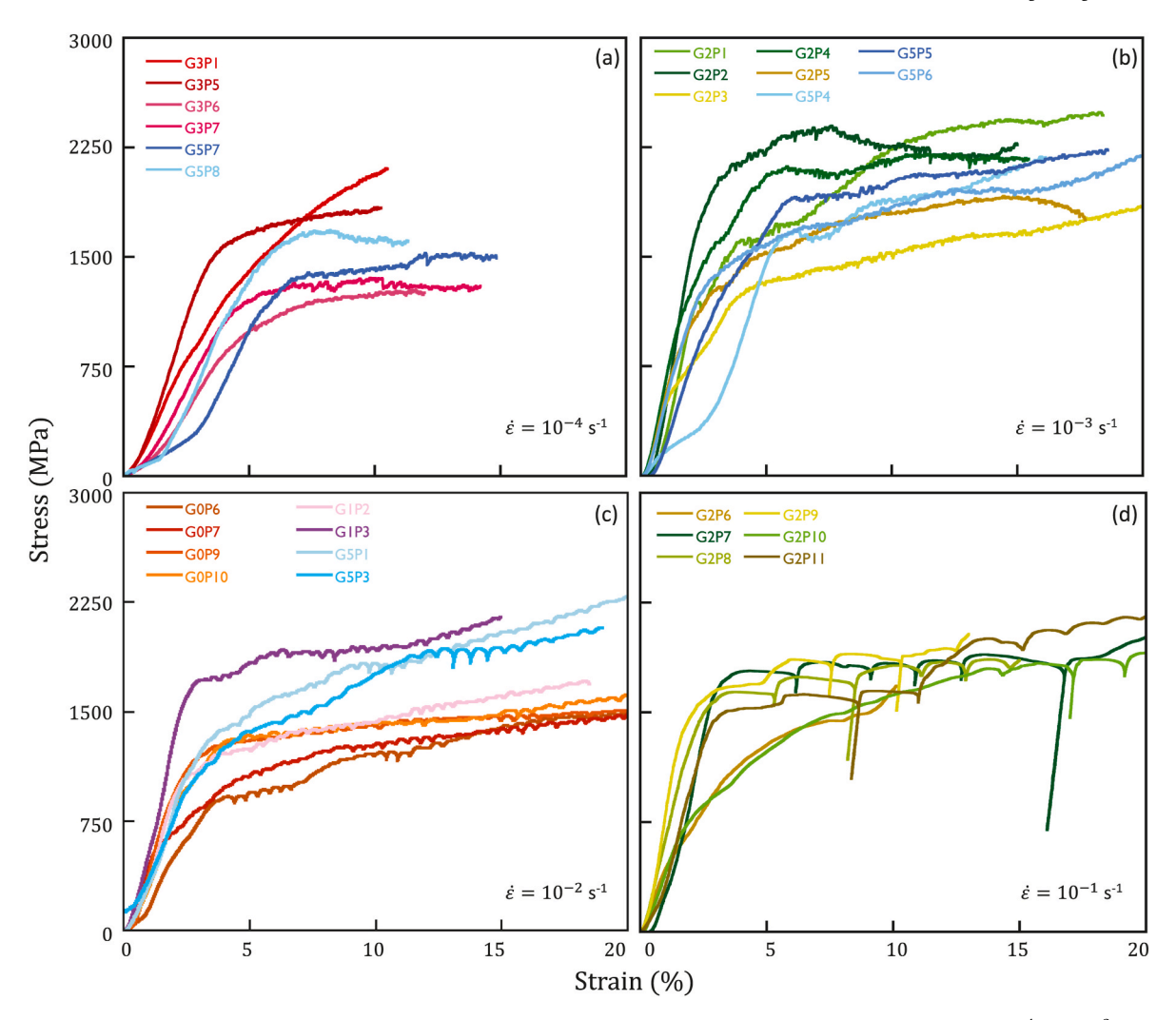


**Fig. 2.** Characteristic stress-strain curves during *in-situ* SEM microcompression tests of RHEA micropillars from different grains at (a)  $10^{-4}$ , (b)  $10^{-3}$ , (c)  $10^{-2}$  and (d)  $10^{-1}$  s<sup>-1</sup> of strain rates. Legend labels as "GxPy" mean Pillar #y from Grain #x.

strongest, group (G2P7, G2P8, G2P9, G2P11) with YS around 1300 MPa and the other (G2P6, G2P10) with an average of 700 MPa. As is commonly observed in this type of tests, load drops characteristic of unstable flow under micropillars compression can be appreciated in almost all conditions [41–43]. The 0.2% offset yield stress values measured from each of stress-strain curves under different strain rates are collected in Table 1. For those stress-strain curves showing a small amount of low-load non-linearity due to the initial misalignment between the micropillar and PicoIndenter tips at the beginning of the microcompression test (specially at lower strain rates), the 0.2% offset yield stress values have been measured from the linear portion of elastic segment after the very initial non-linearity.

Pillars diameter, length and ratio as well as their grain orientation relative to the loading axis are also included in the table. Note that the strength variability for pillars with the same orientation (from the same grain) can be over 500 MPa. See for instance the G3Py case, oriented along the [301] direction, or G0Py oriented along  $[0\overline{1}1]$ .

Fig. 3 shows the critical resolved shear stress,  $(\tau_{CRSS})$  as a function of strain rate for RHEA micropillars from different grains.  $\tau_{CRSS}$  is given by the yield strength multiply by the product of two cosines (Schmid factor) considering  $\overline{n}=[110], \overline{s}=<11\overline{1}>$  since slip generally occurs in specific  $<11\overline{1}>$  directions mainly on the primary  $\{110\}$  crystallographic planes for bcc materials. The colors and labels are the same than those in Fig. 2 for consistency, and the pillar orientation (found using electron diffraction TEM analysis of the compressed pillars), and their

corresponding Schmid factor, m, are also added in the legend. It is clear beyond the scatter in the data that a peak of strength is observed around  $10^{-3} \, \mathrm{s}^{-1}$ . However, pillars soften at  $10^{-2} \, \mathrm{s}^{-1}$  and even more at  $10^{-1} \, \mathrm{s}^{-1}$  resulting in a negative SRS, which may be suggestive of some dynamic strain ageing (DSA) mechanism. This is clearly observed for G5Py oriented along the [211] direction and for G2Py oriented along the [130] direction data points, where a negative SRS is displayed by their average lines in blue and green color, for G5Py and for G2Py, respectively.

#### 3.3. Compositional characterization of RHEA micropillars

In order to explain the scatter found in the strength for micropillars even with the same crystal orientation (from the same grain), we performed a detailed EDS analysis of individual micropillars. Fig. 4 shows representative EDS line profiles along the axial length of some of the strongest pillars tested under compression (shown as insets) at the four strain rates explored. The compositional profiles for all elements show intense fluctuations on a scale on the order of 0.1  $\mu m$ .

A common feature of all plots in Fig. 4 is that the pillars are richest in W in the first half micron of the line profile. The main significance of this observation is that they correspond to the highest measured yield strengths, between 1200 and 1600 MPa. The yield strength values  $(\sigma_{Y})$  for each pillar have added to the plots for reference.

W and Ta distributions follow one another closely at the micropillar tip, possibly indicating an affinity of Ta for W. The same pairing is

**Table 1** Yield stress measurements for each curve shown in Fig. 2.

GxPy	Grain#	Orientation	Pillar#	Pillar diameter (μm)	Pillar Length (µm)	Pillar ratio	Strain rate (1/s)	Yield Stress (MPa)
G0P6	0	[011]	6	0.95	3.59	3.8	0.01	750
G0P7			7	1.01	3.91	3.9	0.01	590
G0P9	U	[OII]	9	0.98	3.59	3.7	0.01	975
G0P10			10	0.98	3.59	3.7	0.01	980
G1P2	1	[311]	2	1.01	3.29	3.3	0.01	975
G1P3			3	1.01	3.36	3.3	0.01	1600
G2P1			1	1.00	3.71	3.7	0.001	1100
G2P2			2	0.97	3.52	3.6	0.001	1600
G2P3			3	0.95	3.86	4.0	0.001	1100
G2P4			4	0.95	3.66	3.9	0.001	914
G2P5			5	1.09	4.46	4.1	0.001	980
G2P6	2	[130]	6	0.99	3.88	3.9	0.1	590
G2P7			7	0.99	3.74	3.8	0.1	1500
G2P8			8	0.98	3.59	3.7	0.1	1300
G2P9			9	1.00	3.69	3.7	0.1	1200
G2P10			10	0.99	3.98	4.0	0.1	720
G2P11			11	0.99	3.54	3.6	0.1	1100
G3P1	3	[301]	1	0.96	3.39	3.5	0.0001	920
G3P5			5	0.95	2.89	3.1	0.0001	1400
G3P6			6	0.99	3.01	3.0	0.0001	910
G3P7			7	0.94	3.22	3.4	0.0001	1100
G5P1			1	1.00	3.66	3.7	0.01	1010
G5P3			3	0.98	2.99	3.1	0.01	1000
G5P4			4	0.99	2.85	2.9	0.001	1600
G5P5	5	[211]	5	0.99	3.26	3.3	0.001	1150
G5P6			6	0.99	3.33	3.4	0.001	1200
G5P7			7	0.99	3.08	3.1	0.0001	1175
G5P8			8	0.94	3.62	3.9	0.0001	1220

<sup>\*</sup>Pillar diameters and lengths with a precision of 10 nm have been added just to discriminate between pillars

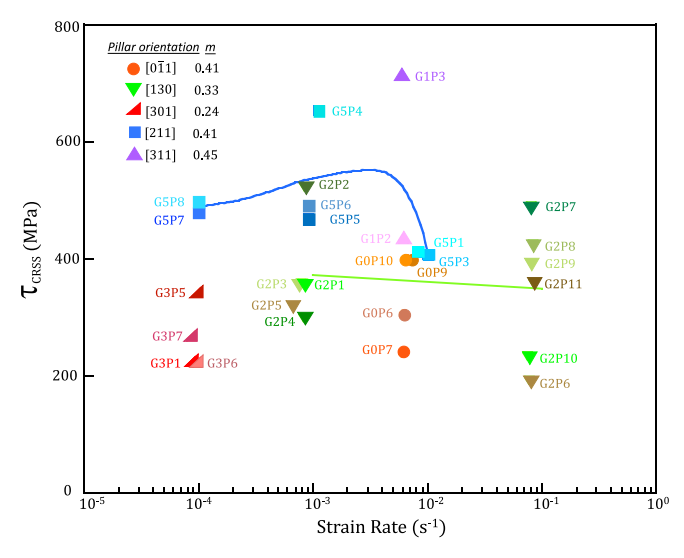


**Fig. 3.** Critical resolved shear stress,  $(\tau_{CRSS})$  as a function of strain rate for RHEA micropillars from different grains. Pillar orientation and their corresponding Schmid factor, m, are also added in the legend.

observed for Nb and Mo. This may suggest the existence of short or medium range order ( $\sim\!0.1~\mu m)$  in the alloy. Those Ta rich regions mainly localized at the bottom of the pillars correspond to the lowest concentration in Nb. These observations are not inconsistent with recent pair interaction calculations, which indeed report repulsive values for Ta–Nb and Mo–W pairs within single crystal Nb–Mo–Ta–W RHEA at room temperature [22,48].

Additionally, a significant increase in Ta concentration along with a decrease gradient of W, Nb and Mo is observed after the half micron tip regions in Fig. 4(b), (c) and (d). This is mainly due to a non-uniform

sample surface induced by the highly deformed tips. Even though these pillars might be Ta-rich below their tip region, it seems like the EDS detector is collecting signals from a thinner sample and because of that the W, Nb and Mo lines decrease while Ta significantly increases to compensate the others. However, those gradients are not observed when the pillar surface is more uniform as shown for instance in Fig. 4a. This is also confirmed by the analysis in Supplementary Fig. S2 where a reduction of those concentration gradients can be seen by performing the EDS line profiles on the same pillar (G1P3) that has been rotated to show a more uniform surface.

By contrast, we have found EDS line profiles that indicate that when Ta appears in a larger proportion near the tip of the pillar, as in Fig. 5a, the average yield strength values drop to around 1000 MPa (consistently at several strain rates as can be seen in Supplementary Fig. S3). Likewise, in those micropillars where Nb is found to be richer in the top region (Fig. 5b), the yield strengths drop even further, to below 600 MPa (see results at different strain rates in Supplementary Fig. S4).

The EDS analysis confirms that spatial fluctuations in the concentration can have a dominant impact on the strength of pillars, at least for micron-sized specimens where the geometric length scale is on the order of the fluctuation wavelength. Remarkably, this holds true independently of strain rate and crystal orientation, demonstrating the dominant effect of chemical composition over all other variables in the tests. As well, the clear correlation existing between strength and stoichiometric abundance must imply that plasticity is governed by dislocation activation or nucleation near the contact region between the picoindenter and the pillar. Again, this is not inconsistent with the SEM images showing a preponderance of plasticity in the top quarter height of all micropillars.

In order to demonstrate the reproducibility in our EDS data, a few additional EDS line profiles were run on the same micropillar (G2P4). As shown in Supplementary Fig. S5, while there is still some scatter in the data, especially for the absolute values of the Ta concentration, the same trend can be observed after four independent runs. In fact, the moving average from the line profiles shows that the tip is rich in Nb and that the

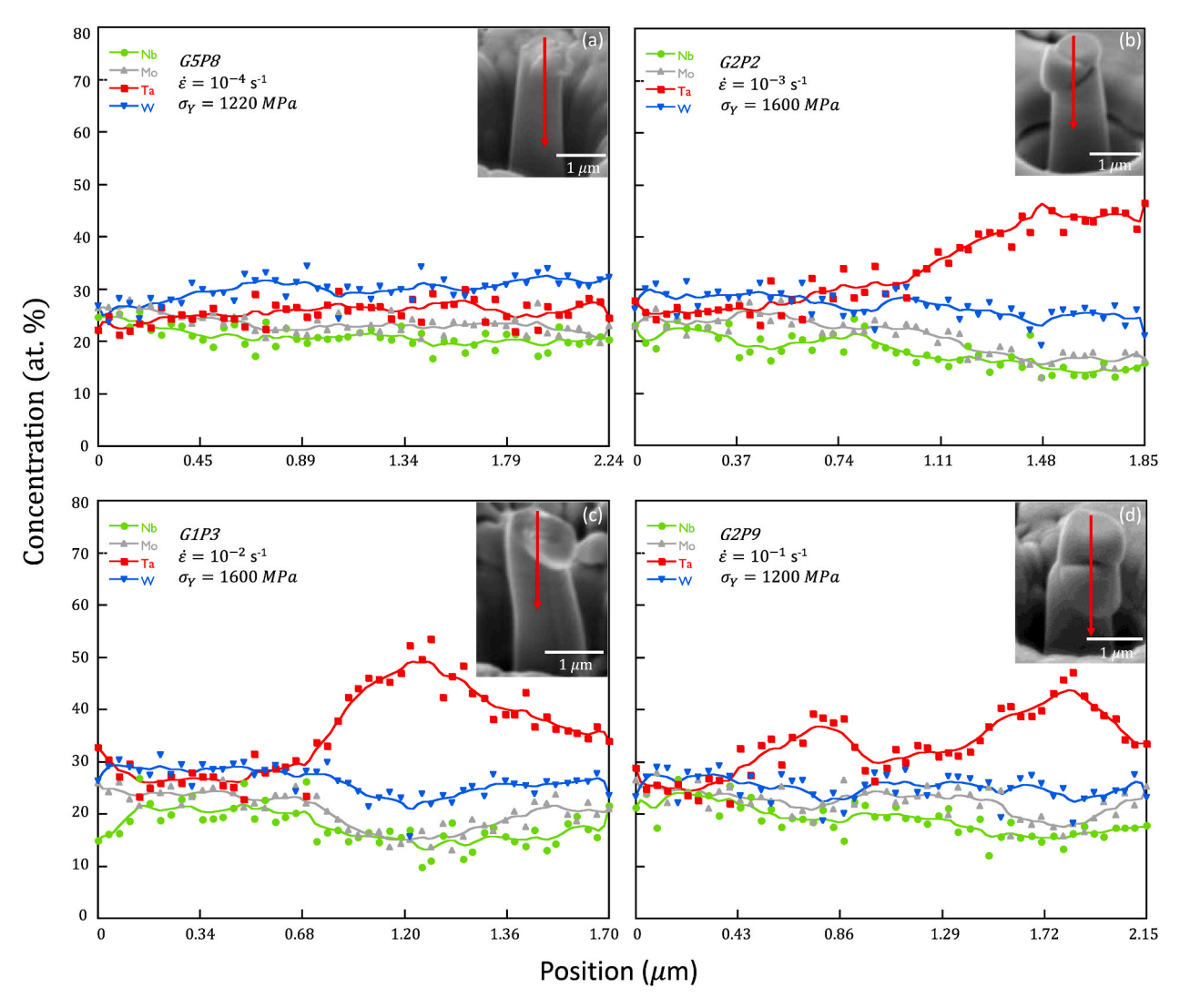


Fig. 4. Line profile EDS analysis along the red arrow from top to bottom of some of the strongest compressed micropillars (insets) from different grains and at different strain rates: (a) G5P8 at  $10^{-4}$  s<sup>-1</sup>, (b) G2P2 at  $10^{-3}$  s<sup>-1</sup>, (c) G1P3 at  $10^{-2}$  s<sup>-1</sup> and (d) G2P9 at  $10^{-1}$  s<sup>-1</sup>. The yield stress values are added in the figure legends. Note that the W concentration is the highest up to 0.5 μm from the pillar tip. (For interpretation of the references to color in this figure legend, the reader is referred to the Web version of this article.)

Mo concentration is very uniform along the entire pillar length. While the W concentration decreases up to 0.9  $\mu m$ , the Ta concentration increases. Once the half-length of the pillar is reached (around 1  $\mu m$ ), it is evident that the Ta concentration is now the highest, while the Nb one decreases to meet the W and Mo line profiles near the stoichiometric concentration. These results prove that the variations shown by the moving averages are not only due to the signal noise but also due to the compositional fluctuations in our sample.

Finally, we performed a detailed *post-mortem* TEM characterization of at least one deformed micropillar within each grain. By way of example, the TEM analysis of a representative compressed micropillar (G0P9) is shown in Fig. 6. Fig. 6a and b shows  $52^{\circ}$  tilted-view SEM images of the micropillar before and after compression. Shear bands are clearly apparent on the micropillar surface approximately parallel to each other (Fig. 6b). A TEM thin slice was created by FIB from side cross-sectional view of this micropillar and the bright-field TEM image is shown in Fig. 6c. Its selected area electron diffraction (SAED) pattern as inset oriented to the [011] zone axis verifies the bcc single phase structure of a pillar oriented along the [011] direction. No secondary phases or phase transformation during deformation were found.

From an atomic resolution TEM image (Fig. 6d), an edge dislocation dipole separated around 2 nm is lying on the ((200) plane as shown by

its FFT (inset). The FFT also shows a slightly rotated (4°) lattice with respect to the SAED pattern (inset in Fig. 6c) indicating that the tip is slightly rotated with respect to the middle part of the pillar as a consequence of the deformation. The presence of edge dislocations is a remarkable finding, given that the deformation is generally accepted to be controlled by screw dislocations in bcc metals and alloys [17,32–35]. Edge dislocations are profusely observed in several of the other grains as well. For example, in Grain #5 (which is oriented to the [211] direction), a collection of edge dislocations on several  $\{1\overline{1}2\}$  planes can be clearly detected in the high resolution micrograph shown in Fig. 7. Our observation is consistent with both  $\{110\}$  and  $\{112\}$  being common slip planes in bcc systems [49].

#### 4. Discussion

Our main results concern two relatively new aspects of RHEA mechanical behavior: (i) characterizing the quantitative link between strength and local composition, and (ii) the prolific observation of edge dislocations in the deformed microstructure. We center the following discussion around these main two points.

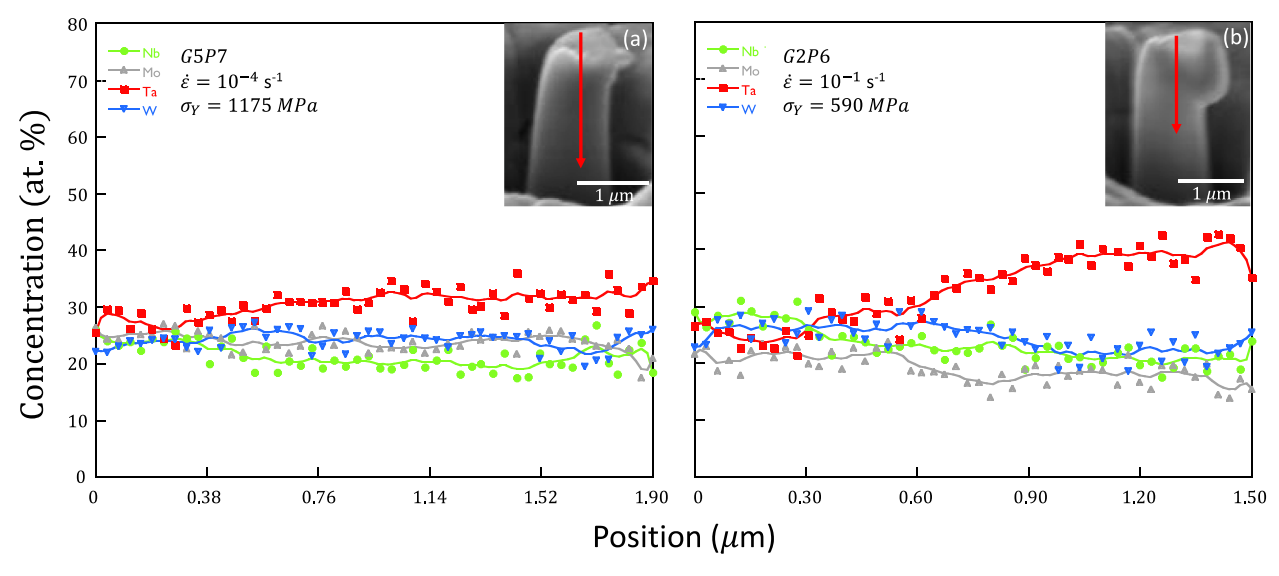


Fig. 5. Line profile EDS analysis along the red arrow from top to bottom of some of the compressed micropillars (insets) with the top rich in Ta (a) and Nb (b). (For interpretation of the references to color in this figure legend, the reader is referred to the Web version of this article.)

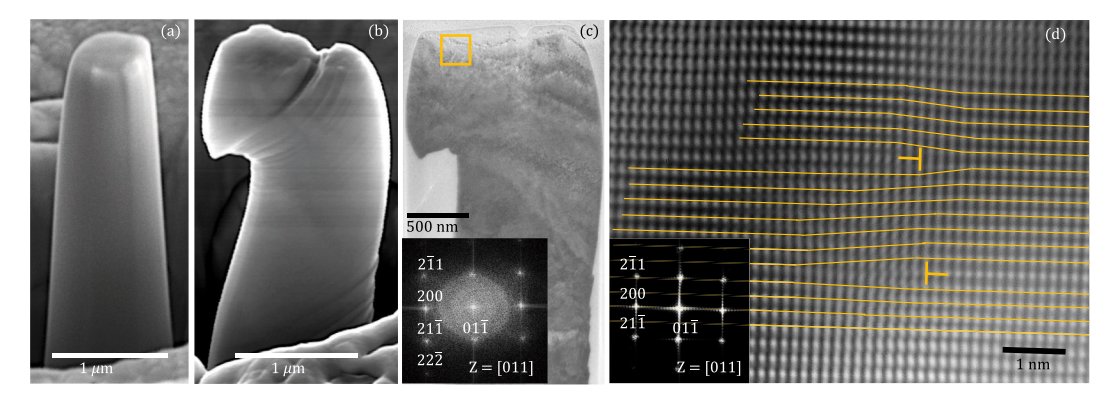


Fig. 6. (a) and (b) SEM images of the GOP9 micropillar before and after compression. (c) TEM image of the compressed micropillar in (b) and its SAED pattern shown as inset. (d) Fourier filtered atomic resolution TEM image from the region highlighted by a yellow square showing a pair of edge dislocations on the ((200)) planes. Inset is the FFT of the image. (For interpretation of the references to color in this figure legend, the reader is referred to the Web version of this article.)

#### 4.1. RHEA micropillar strength

The strength of micropillars extracted from different grains displays the standard orientation dependence attributable to the Schmid projection. Fig. 3 shows the critical resolved shear stress ( $\tau_{CRSS}$ ) as a material property that does not depend on the applied load or grain orientation as a function of the strain rate. However, our results show some scatter in the data even for micropillars from the same grain (same orientation). This is the case for instance of G1P3 with the [311] orientation, which is seen to be stronger than the rest in agreement with Schmid's law. In contrast, the CRSS for another micropillar from the same grain, G1P2, is around 300 MPa lower. Since the CRSS should not change much for the same slip system, the scatter found for micropillars even from the same grain cannot be explained only by the Schmid's law but also due to local composition fluctuations. As shown by the EDS analysis of both micropillars, G1P3 has a W-rich tip that leads to a yield strength of 1600 MPa (Fig. 4c) while G1P2 presents a Ta-rich tip with a yield strength of 975 MPa (Fig. S3c).

Nevertheless, it is clear beyond the scatter in the data that a peak of strength is observed around  $10^{-3}\,\mathrm{s}^{-1}$ . Likewise, micropillars consistently soften at  $10^{-2}\,\mathrm{s}^{-1}$  and then further soften at  $10^{-1}\,\mathrm{s}^{-1}$ . A negative SRS –or at least a saturation of it– can be unequivocally appreciated. This can now be clearly seen for the G5Py (oriented along the [211] direction) and for G2Py (oriented along the [130] direction) data points, where a

negative SRS is displayed by their average lines in blue and green color, for G5Py and for G2Py, respectively. We also segregate the data by micropillar crystallographic orientation in Supplementary Fig. S6. For example, the softest micropillar's strength peaks at 1219  $\pm$  41 MPa at  $10^{-3}$  s<sup>-1</sup>, followed by a value of  $1005 \pm 88$  MPa at  $10^{-2}$  s<sup>-1</sup>. Negative SRS is also observed if we consider all the stress-strain curves for G5Pv micropillars at different strain rates. An average of 1200  $\pm$  32 MPa is obtained at  $10^{-4}$  s<sup>-1</sup>, while a peak strength of 1317  $\pm$  247 MPa and followed by a value of  $1005 \pm 7$  MPa are measured at  $10^{-3} \, s^{-1}$  and  $10^{-2}$ s<sup>-1</sup>, respectively. The negative SRS may be suggestive (not proof of) of some dynamic strain ageing (DSA) mechanism, as observed in smallscaled NbMoTaW RHEA pillars [26,36] and in other material systems [42–55]. Given the fact that these alloys are known to display sluggish self-diffusion even at high temperatures, the observed behavior may be related to a diffusion-less process such as -perhaps- breakage of short-range order (SRO) or due to interstitial impurity atmospheres (which form athermally), although at the moment this is speculative.

In addition to that multicomponent random alloys introduce a new paradigm due to their high compositional complexity and varied atomic chemical interactions. In such environments, even the standard strengthening processes commonly found in bcc metals cannot explain the mechanical behavior of these systems. New plastic mechanisms are being proposed on the basis of new experimental and theoretical/computational evidence [17,32,33,56] that confirm the large influence

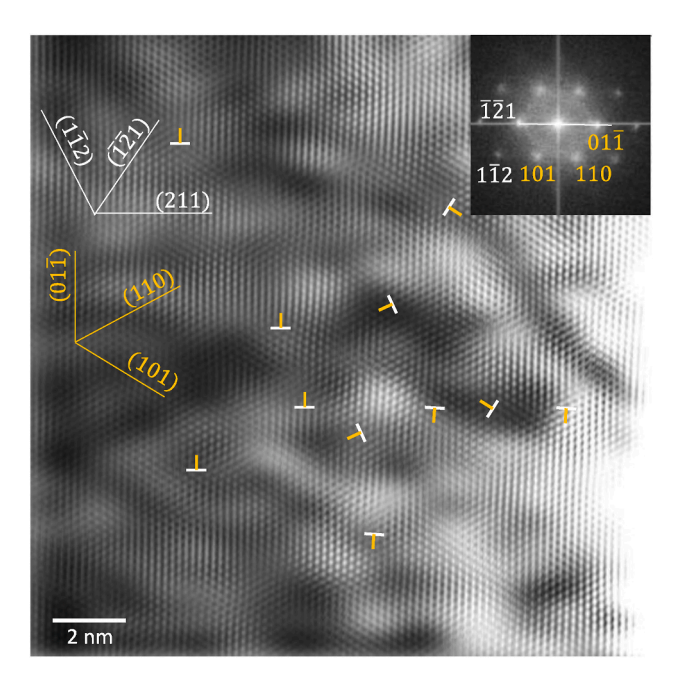


Fig. 7. Fourier filtered atomic resolution TEM image of a compressed pillar from Grain #5 showing a significant number of edge dislocations on the  $\{1\overline{1}2\}$  planes (highlighted in white) with the extra planes parallel to  $\{011\}$  planes (highlighted in yellow). FFT of the image (inset) indicating the  $<\overline{1}11>$  zone axis. (For interpretation of the references to color in this figure legend, the reader is referred to the Web version of this article.)

of local chemistry on deformation processes. We believe that the chemical composition near the micropillar tip is the best quantitative predictor of yield strength over strain rate, grain orientation or any other experimental issues, if any (no misalignment or significant local friction was found during our tests). In particular, we measured a yield strength of 1500 MPa in micropillars tip rich in W, while for those with a Ta and Nb-rich oscillations, the yield strength was 1000 and 700 MPa, respectively.

As such, the strength of the micropillars is clearly dominated by the strength of the preponderant element in that region. This is a strong indication that compositional fluctuations in these specimens exacerbate the nonuniformity of the spatial stress distribution in the micropillars.

We also report from evidence in all micropillars that the compositional fluctuations are characterized by the pairs Ta–W and Nb–Mo evolving in sync (and counter to one another). This is consistent with recent atomistic calculations [48] and may be a manifestation of the existence of SRO reported in other works [9,22].

Although microcompression testing is not the best method to measure the elastic modulus, we also find differences in the slope of the stress-strain curves from different micropillars even from the same grain. In particular, we find that softer micropillars show almost two-times lower slope (indicating less stiff material) than stronger micropillars. As reported by Zabransky et al. [57] minor geometrical differences between micropillars such as a slightly higher tapering angle can lead to lower elastic modulus. However, since the measured tapering angles were  $<5^{\circ}$ , we speculate that the differences in the slope (elastic modulus) could be also due to the large variations in composition between micropillars even from the same grain.

#### 4.2. Presence of edge dislocations

To date, the unusually high strength observed in several RHEA, including the Nb-Mo-Ta-W system [9,18,19,26,27,30,32-34,48], has not been conclusively correlated to a specific dislocation type or

mechanism. As it relates to screw dislocations, which are responsible for plastic flow in bcc metals and alloys, several features related to kink-pair nucleation and kink propagation have been identified as being uniquely modified by complex and rapidly varying chemical environments [17, 32–35]. A consensus is emerging about the recognition of the enhanced role that cross-kinks appear to play in screw dislocation slip [32–35]. Indirect evidence of this mechanism is the observation of trailing prismatic loops during screw dislocation motion, which form after the closing of cross-kinks [31,56].

However, recent evidence points also to the increased role of edge dislocations as vehicles of deformation [48,58,59] in NbMoTaW or similar bcc RHEA [60]. The existence of edge dislocations can be usually correlated to the existence of large lattice distortions. Our EDS analysis appears to confirm this general idea, where large lattice distortions lead to enhanced edge dislocation activity.

X-ray diffraction techniques should be used as Moorehead et al. [61] and Zhang et al. reported [62] in order to measure the lattice parameter accurately. However, as shown by Senkov et al. [63] the standard rule of mixtures is notoriously violated in RHEA, and that might be an indication of some distortion in the range of interatomic distances. As reported by Zhang et al. [64], since the atomic sizes of Nb and Ta are around 5% larger than Mo and W, an intrinsic lattice distortion effect caused by the addition of multi-principal elements with different atomic sizes is expected. This atomic size misfit of the constituent elements in the HEA can cause a highly distorted lattice [19]. This is basically due to the interaction energies between some atomic pairs that are lower than in others. Therefore, some atomic pair configurations are more energetically favorable, resulting in a much greater number of lower energy configurations than in the completely random case.

The existence of the aforementioned lattice distortions may be a necessary condition for the presence of edge dislocations, but not the only one. The other is the existence of similar edge and screw dislocation mobilities, so that both characters contribute to plasticity and can be observed during deformation. The standard picture of bcc-metal plasticity, screw dislocation glide is the rate-controlling mechanism for slip [65]. This is because generally, edge dislocations with their extended planar cores display a high mobility at all stresses, particularly at low and intermediate temperatures. However, a new picture is starting to emerge for RHEA whereby edge dislocations display similar mobilities to screw dislocations. This seems to be due to the existence of large lattice distortions and atomistic misfit, which negates the planar structure of edge dislocations and slows them down relative to their pure metal or dilute alloy counterparts. By using atomistic simulations [48], edge and screw dislocation mobilities have been reported to be similar so that both characters contribute to plasticity and can be observed during deformation in NbMoTaW RHEA. This means that both dislocations now play a role in RHEA plasticity, acting as obstacles to one another or by complementing one another during plastic flow. Indeed, in our experiments, we observe edge dislocations before, during and after deformation, confirming their primary role as carriers of plasticity.

In any case, the strong correlation between chemical composition near the micropillar tip and micropillar strength strongly suggests that the governing mechanism is related to a Peierls type activation of edge or screw dislocations in the region around the tip, without discarding the possibility of nucleation. It is well known that the yield strength correlates with dislocation critical glide stress (e.g., the Peierls stress for screw dislocations). As reported by Dezerald et al. [66] the values of the Peierls stress for the main bcc metals are 900 and 870 MPa for W and Mo, while 450 and 350 MPa for the softest Nb and Ta, respectively. While this correlation may not be as clear-cut for edge dislocations, it is reasonable to assume that it follows the same trends. As such, the strongest micropillars display a strength consistent with a dominant composition of W, while the softest are for Ta and Nb.

#### 5. Conclusions

In summary, we report for the first time that the strength of bcc NbMoTaW RHEA micropillars can be controlled by their local chemical composition. We use EDS line profile analysis on compressed micropillars after in-situ SEM microcompression tests at room temperature between 10<sup>-4</sup> to 10<sup>-1</sup> s<sup>-1</sup> of strain rate. Our results lead us to conclude that independently of the strain rate or crystal orientation, a yield strength around 1500 MPa can be reached for micropillars rich in W. For those Ta rich micropillars their yield strength is around 1000 MPa while for those Nb rich in composition this value is much lower around 800 MPa. It is clear beyond the scatter in the data that a peak of strength is observed around  $10^{-3}$  s<sup>-1</sup> resulting in a negative SRS for higher strain rates. We attribute the negative SRS to the DSA mechanism, which is typically accepted as a sufficient condition for serrated flow. Additionally, our EDS results have suggested Ta-W and Nb-Mo as the most energetically favorable atomic pairs, which is indicative of a SRO in the lattice. Finally, using atomic resolution TEM, we have identified a great number of edge dislocations on the {112} planes after compression. We believe that the local composition fluctuations found by the EDS analysis create a large density of lattice mismatch points that might be responsible of the stability of edge dislocations during the plastic deformation of the NbMoTaW RHEA micropillars at room temperature.

#### CRediT authorship contribution statement

**Marta Pozuelo:** Conceptualization, Methodology, Investigation, Formal analysis, Writing – original draft, Writing – review & editing. **Jaime Marian:** Conceptualization, Formal analysis, Supervision, Project administration, Writing – review & editing.

#### Declaration of competing interest

The authors declare that they have no known competing financial interests or personal relationships that could have appeared to influence the work reported in this paper.

#### Data availability

Data will be made available on request.

#### Acknowledgements

This work was funded by NSF, Metals and Metallic Nanostructures Program, under grant DMR- 1905822. The authors are particularly grateful to Noah Bodzin for his continuous support with the TEM samples preparation by FIB. They are also grateful to the anonymous referees for their insightful remarks.

#### Appendix A. Supplementary data

Supplementary data to this article can be found online at https://doi.org/10.1016/j.msea.2022.143892.

#### References

- B. Cantor, I.T.H. Chang, P. Knight, A.J.B. Vincent, Microstructural development in equiatomic multicomponent alloys, Mater. Sci. Eng. 375–377 (2004) 213–218.
- [2] J.-W. Yeh, S.-K. Chen, S.-J. Lin, J.-Y. Gan, T.-S. Chin, T.-T. Shun, C.-H. Tsau, S.-Y. Chang, Nanostructured high-entropy alloys with multiple principal elements: novel alloy design concepts and outcomes, Adv. Eng. Mater. 6 (2004) 299–303.
- [3] J.-W. Yeh, Recent progress in high entropy alloys, Ann. Chim. Sci. Mat. 31 (2006) 633–648.
- [4] J.-W. Yeh, Y.L. Chen, S.J. Lin, S.K. Chen, High-entropy alloys—a new era of exploitation, Mater. Sci. Forum 560 (2007) 1–9.
- [5] E.J. Pickering, N.G. Jones, High-entropy alloys: a critical assessment of their founding principles and future prospects, Int. Mater. Rev. 61 (2016) 183–202.
- [6] M.C. Gao, J.-W. Yeh, P.K. Liaw, Y. Zhang, High-Entropy Alloys, Springer International Publishing, 2016.

- [7] D.B. Miracle, O.N. Senkov, A critical review of high entropy alloys and related concepts, Acta Mater. 122 (2017) 448–511.
- [8] M.-H. Tsai, J.-W. Yeh, High-entropy alloys: a critical review, Mater. Res. Letters 2 (2014) 107–123.
- [9] O. Senkov, D. Miracle, K. Chaput, J. Couzinie, Development and exploration of refractory high entropy alloys–A review, J. Mater. Res. 33 (2018) 3092–3128.
- [10] M. Gao, J. Qiao, High-entropy alloys (HEAs), Metals 8 (2018) 108-110.
- [11] B. Gludovatz, A. Hohenwarter, D. Catoor, E.H. Chang, E.P. George, R.O. Ritchie, A fracture-resistant high-entropy alloy for cryogenic applications, Science 345 (2014) 1153–1158.
- [12] D.B. Miracle, J.D. Miller, O.N. Senkov, C. Woodward, M.D. Uchic, J. Tiley, Exploration and development of high entropy alloys for structural applications, Entropy 16 (2014) 494–525.
- [13] Y. Zhang, T.T. Zuo, Z. Tang, M.C. Gao, K.A. Dahmen, P.K. Liaw, Z.P. Lu, Microstructures and properties of high-entropy alloys, Prog. Mater. Sci. 61 (2014) 1–93.
- [14] L. Lilensten, J.-P. Couzinié, L. Perrière, A. Hocini, C. Keller, G. Dirras, I. Guillot, Study of a bcc multi-principal element alloy: tensile and simple shear properties and underlying deformation mechanisms, Acta Mater. 142 (2018) 131–141.
- [15] S.I. Rao, C. Varvenne, C. Woodward, T.A. Parthasarathy, D. Miracle, O.N. Senkov, W.A. Curtin, Atomistic simulations of dislocations in a model BCC multicomponent concentrated solid solution alloy, Acta Mater. 125 (2017) 311–320.
- [16] W.Y. Wang, S.L. Shang, Y. Wang, F. Fengbo K.A. Darling, Y. Wu, X. Xie, O. N. Senkov, J. Li, X.D. Hui, K.A. Dahmen, P.K. Liaw, L.J. Kecskes, Z.-K. Liu, Atomic and electronic basis for the serrations of refractory high-entropy alloys, npj Comp. Mater. 23 (2017) 1–10.
- [17] H. Dobbelstein, M. Thiele, E.L. Gurevich, E.P. George, A. Ostendorf, Direct metal deposition of refractory high entropy alloy MoNbTaW, Phys. Procedia 83 (2016) 624–633
- [18] O.N. Senkov, G.B. Wilks, J.M. Scott, D.B. Miracle, Mechanical properties of Nb25Mo25Ta25W25 and V20Nb20Mo20Ta20W20 refractory high entropy alloys, Intermetallics 19 (2011) 698–706.
- [19] Y. Zou, S. Maiti, W. Steurer, R. Spolenak, Size-dependent plasticity in an Nb25Mo25Ta25W25 refractory high-entropy alloy, Acta Mater. 65 (2014) 85–97.
- [20] H. Yao, J.-W. Qiao, M.C. Gao, J.A. Hawk, S.-G. Ma, H. Zhou, MoNbTaV medium-entropy alloy, Entropy 18 (2016) 189–204.
- [21] F. Körmann, M.H.F. Sluiter, Interplay between lattice distortions, vibrations and phase stability in NbMoTaW high entropy alloys, Entropy 18 (2016) 403–500.
- [22] A. Fernandez-Caballero, J.S. Wrobel, P.M. Mummery, D. Nguyen-Manh, Short-range order in high entropy alloys: theoretical formulation and application to Mo-Nb-Ta-V-W system, J. Phase Equilibria Diffus. 38 (2017) 391–403.
- [23] X.B. Feng, J.Y. Zhang, Y.Q. Wang, Z.Q. Hou, K. Wu, G. Liu, J. Sun, Size effects on the mechanical properties of nanocrystalline NbMoTaW refractory high entropy alloy thin films, Int. J. Plast. 95 (2017) 264–277.
- [24] X. Feng, J. Zhang, Z. Xia, S. Sun, Stable nanocrystalline NbMoTaW high entropy alloy thin films with excellent mechanical and electrical properties, Mater. Lett. 210 (2017) 84–87.
- [25] F. Koermann, A.V. Ruban, M.H.F. Sluiter, Long-ranged interactions in bcc NbMoTaW high-entropy alloys, Mater. Res. Letters 5 (2017) 35–40.
- [26] Y. Zou, H. Ma, R. Spolenak, Ultrastrong ductile and stable high-entropy alloys at small scales, Nat. Commun. 6 (2015) 7748.
- $\hbox{\bf [27]}\ \ Y.\ Zou,\ Nanomechanical\ studies\ of\ high-entropy\ alloys,\ J.\ Mater.\ Res.\ (2018)\ 1-20.$
- [28] D. Kaufmann, R. Monig, C.A. Volkert, O. Kraft, Size dependent mechanical behaviour of tantalum, Int. J. Plast. 27 (2011) 470–478.
- [29] Q. Ding, Y. Zhang, X. Chen, X. Fu, D. Chen, S. Chen, L. Gu, F. Wei, H. Bei, Y. Gao, M. Wen, J. Li, Z. Zhang, T. Zhu, R.O. Ritchie, Q. Yu, Tuning element distribution, structure and properties by composition in high-entropy alloys, Nature 574 (2019) 223–227.
- [30] Z. Lei, Xiongjun Liu, Y. Wu, H. Wang, S. Jiang, S. Wang, X. Hui, Y. Wu, B.P. Gault, Kontis, D. Raabe, L. Gu, Q. Zhang, H. Chen, H. Wang, J. Liu, K. An, Q. Zeng, T.-G. Nieh, Z. Lu, Enhanced strength and ductility in a high-entropy alloy via ordered oxygen complexes. Nature 563 (2018) 546–550.
- [31] Y. Bu, Y. Wu, Z. Lei, X. Yuan, H. Wu, X. Feng, J. Liu, J. Ding, Y. Lu, H. Wang, Z. Lu, W. Yang, Local chemical fluctuation mediated ductility in body-centered-cubic high-entropy alloys, Mater. Today 46 (2021) 28–34.
- [32] X. Zhou, S. He, J. Marian, Cross-kinks control screw dislocation strength in equiatomic bcc refractory alloys, Acta Mater. 211 (2021), 116875.
- [33] S. Yin, Y. Zuo, A. Abu-Odeh, H. Zheng, S.G. Li, J. Ding, S.P. Ong, M. Asta, R. O. Ritchie, Atomistic simulations of dislocation mobility in refractory high-entropy alloys and the effect of chemical short-range order, Nat. Commun. 12 (2021) 1–14.
- [34] E.P. George, W.A. Curtin, C.C. Tasan, High entropy alloys: a focused review of mechanical properties and deformation mechanisms, Acta Mater. 188 (2020) 435–474.
- [35] J. Marian, W. Cai, V.V. Bulatov, Dynamic transitions from smooth to rough to twinning in dislocation motion, Nat. Mater. 3 (2004) 158–163.
- [36] Yong Zhang, Jun Peng Liu, Shu Ying Chen, Xie Xie, Peter K. Liaw, Karin A. Dahmen, Jun Wei Qiao, Yan Li Wang, Serration and noise behaviors in materials, Prog. Mater. Sci. 90 (2017) 358–460.
- [37] S.V. Prikhodko, I. Kakoulli, in: Sandra L. López Varela (Ed.), The Encyclopedia of Archaeological Sciences, John Wiley & Sons, Inc., 2018, 2018 by John Wiley & Sons, Inc.
- [38] K. Kanaya, S. Okayama, Penetration and energy-loss theory of electrons in solid targets, J. Phys. D Appl. Phys. 5 (1972) 43–58.
- [39] H. Zhang, B.E. Schuster, Q. Wei, K.T. Ramesh, Scripta Mater. 54 (2006) 181-186.
- [40] S. Shim, H. Bei, M.K. Miller, G.M. Pharr, E.P. George, Acta Mater. 57 (2009) 503–510.

- [41] M. Pozuelo, Y.W. Chang, J. Marian, J.M. Yang, Serrated flow in nanostructured binary Mg-Al alloys, Scripta Mater. 127 (2017) 178–181.
- [42] M. Pozuelo, J.W. Stremfel, J.-M. Yang, J. Marian, Strengthening to softening transition in lath martensite, Materialia 5 (2019), 100254.
- [43] M. Pozuelo, K. Jiang, J. Marian, Separation of time scales of plastic instabilities during microscale deformation of bcc Fe, Met. Mater. Trans. A 52 (2021) 4275–4289.
- [44] Y.W. Chang, M. Pozuelo, J.-M. Yang, Mater. Res. Lett. 2 (2014) 199-203.
- [45] M. Pozuelo, Y.W. Chang, J.-M. Yang, Mater. Sci. Eng., A 594 (2014) 203-211.
- [46] M. Pozuelo, Y.-W. Chang, J.-M. Yang, Mater. Sci. Eng., A 633 (2015) 200-208.
- [47] L.-Y. Chen, J.-Q. Xu, H. Choi, M. Pozuelo, X. Ma, S. Bhowmick, J.-M. Yang, S. Mathaudhu, X.-C. Li, Nature 528 (2015) 539–543.
- [48] X.-G. Li, C. Chen, H. Zheng, Y. Zuo, S.P. Ong, Complex strengthening mechanisms in the NbMoTaW multi- principal element alloy, npj Comp. Mater. 6 (2020) 70.
- [49] C.R. Weinberger, B.L. Boyce, C.C. Battaile, Slip planes in bcc transition metals, 5, Int. Mater. Reviews 58 (2013) 296–314.
- [50] A.H. Cottrell, A note on the portevin-le chatelier effect, Philos. Mag. A 44 (1953) 829-832.
- [51] C. Corby, C.H. Cáceres, P. Luká, Serrated flow in magnesium alloy AZ91, Mater. Sci. Eng., A 387 (2004) 22–24.
- [52] C. Wang, Y. Xu, E. Han, Serrated flow and abnormal strain rate sensitivity of a magnesium-lithium alloy, Mater. Lett. 60 (2006) 2941–2944.
- [53] S.K. Wu, C. Chien, C.S. Yang, H.Y. Bor, The portevin–le chatelier effect in β-phase Mg–14.3Li–0.8 Zn alloy, Mater. Sci. Eng., A 605 (2014) 33–38.
- [54] R.C. Picu, A mechanism for the negative strain-rate sensitivity of dilute solid solutions, Acta Mater. 52 (2004) 3447–3458.

- [55] L. Jiang, J.J. Jonas, R. Mishra, Effect of dynamic strain aging on the appearance of the rare earth texture component in magnesium alloys, Mater. Sci. Eng., A 528 (2011) 6596–6605.
- [56] D. Caillard, A TEM in situ study of alloying effects in iron. II—solid solution hardening caused by high concentrations of Si and Cr, Acta Mater. 61 (2013) 2808–2827.
- [57] L. Zábranský, K. Bernátová, J. Dluhoš, R. Váňa, Pavel Souček, P. Vašina, V. Buršíková, Materials 13 (2020) 3054–3065.
- [58] L. Zhao, H. Zong, X. Ding, T. Lookman, Anomalous dislocation core structure in shock compressed bcc high-entropy alloys, Acta Mater. 209 (2021), 116801.
- [59] C. Lee, F. Maresca, Rui Feng, Y. Chou, T. Ungar, M. Widom, K. An, J.D. Poplawsky, Y.-C. Chou, P.K. Liaw, W.A. Curtin, Strength can be controlled by edge dislocations in refractory high-entropy alloys, Nat. Commun. 12 (2021) 5474.
- [60] S. Xu, Y. Su, W.-R. Jian, I.J. Beyerlein, Local slip resistances in equal-molar MoNbTi multi-principal element alloy, Acta Mater. 202 (2021) 68–79.
- [61] M. Moorehead, K. Bertsch, M. Niezgoda, C. Parkin, M. Elbakhshwan, K. Sridharan, C. Zhang, D. Thoma, A. Couet, Mater. Des. 187 (2020), 108358.
- [62] H. Zhang, Y. Zhao, S. Huang, S. Zhu, F. Wang, D. Li, Materials 12 (2019) 720.
- [63] O.N. Senkov, G.B. Wilks, D.B. Miracle, C.P. Chuang, P.K. Liaw, Refractory high-entropy alloys, Intermetallics 18 (2010) 1758–1765.
- [64] Y. Zhang, T.T. Zuo, Z. Tang, M.C. Gao, K.A. Dahmen, P.K. Liaw, Z.P. Lu, Prog. Mater. Sci. 61 (2014) 1–93.
- [65] W. Cai, V.V. Bulatov, J.-P. Chang, J. Li, S. Yip, Dislocation core effects on mobility, chap. 64, in: F.R.N. Nabarro, J.P. Hirth (Eds.), Dislocations in Solids, vol. 12Elsevier, Amsterdam, 2004, pp. 1–80. ISBN 044451483X.
- [66] L. Dezerald, Lisa Ventelon, E. Clouet, C. Denoual, D. Rodney, F. Willaime, Ab initio modeling of the two-dimensional energy landscape of screw dislocations in bcc transition metals, Phys. Rev. B 89 (2014), 024104.